

“© 20XX IEEE. Personal use of this material is permitted. Permission from IEEE must be obtained for all other uses, in any current or future media, including reprinting/republishing this material for advertising or promotional purposes, creating new collective works, for resale or redistribution to servers or lists, or reuse of any copyrighted component of this work in other works.”

A Droop based Adaptive Power Management System for Energy Storage Integration to DC Grid using a Modified Dual Active Bridge Converter

Sanjib Kumar Mitra, Student Member, IEEE, and Srinivas Bhaskar Karanki,
Senior Member, IEEE

The authors are with the School of Electrical Sciences, Indian Institute of Technology Bhubaneswar, Bhubaneswar 752050, India (e-mail: skm19@iitbbs.ac.in; skaranki@iitbbs.ac.in).

This work was financially supported by the Department of Science and Technology (DST), India and the European Union's Horizon 2020 Research and Innovation Program through the RE-EMPOWERED Project under Grant Agreement No DST/TMD/INDIA/EU/ILES/2020/50(c) and 101018420 respectively.

Digital Object Identifier 10.1109/JESTPE.2022.3225379

A Droop based Adaptive Power Management System for Energy Storage Integration to DC Grid using a Modified Dual Active Bridge Converter

Sanjib Kumar Mitra, *Student Member, IEEE*, and Srinivas Bhaskar Karanki, *Senior Member, IEEE*

Abstract—This article proposes an adaptive power Management system for energy storage integration to the DC grid using a modified dual active bridge bi-directional DC-DC converter. The converter can achieve high voltage gain and zero voltage switching for a wide range of loading conditions with distributed voltage stress. An adaptive power Management system (APMS) is designed with a voltage droop control based model reference adaptive control (MRAC). A reduced order harmonic model of the converter is used for the APMS design. The proposed APMS does not require detailed knowledge of the system parameters and is also robust to uncertainty and multiple disturbances. The proposed converter and its control technique are verified in MATLAB/SIMULINK platform. An experimental laboratory prototype is also developed for 500W rating, and the results are presented to validate the system's efficacy by comparing with conventional PI and sliding mode controllers.

Index Terms—DC-DC converter, dual active bridge converter, energy storage integration, model reference adaptive control, adaptive power management system.

| | |
|-------------|---|
| m | Harmonic order |
| Z | Impedance of the HFT referred to LV side |
| T_d | Dead time of switching pulse |
| v_m | Reference model output voltage |
| v_r | Reference model input |
| a_m, b_m | Reference model parameter |
| W_m | Reference model |
| e | Error between reference model output voltage and actual plant voltage |
| a_p, b_p | Plant model parameter |
| a_r, a_y | Control Parameter |
| J | Lyapunov function |
| γ | Adaptive gain |
| K_{droop} | Voltage droop constant |

NOMENCLATURE

| | |
|-------------------|---|
| P | Power requirement |
| v_{Batt} | Input battery voltage |
| v_{dc} | DC link voltage |
| V_{dcnom} | Nominal DC link voltage |
| R_L | Winding resistance of the HFT referred to LV side |
| L_r | Leakage inductance of the HFT referred to LV side |
| $\frac{N_p}{N_s}$ | High frequency transformer turns ratio |
| v_{LV} | Low winding voltage |
| v_{HV} | High winding voltage |
| i_{LV} | Low voltage winding current |
| i_{HV} | High voltage winding current |
| C_A | Input capacitor |
| C_s | Switch parasitic capacitance |
| $C_{B1,2}$ | Output capacitor |
| $= C$ | |
| δ | Phase shift angle |
| ω | Angular switching frequency |
| f_s | Switching frequency |
| R_{load} | Load resistance |

I. INTRODUCTION

THE gradual depletion of fossil fuel reserves is reducing global power generation, whereas the power demand is rising continuously. The mismatch between generation and demand imposes a power crisis issue across the globe. In this scenario, renewable energy sources (RES) like PV and wind are promising alternatives due to their abundance in nature, and also they are pollution-free energy sources [1], [2]. However, these energy sources are intermittent due to their dependency on weather conditions, which further degrades the quality of generated power [3], [4]. This problem can be resolved by using energy storage devices (ESD) alongside RES [5].

RES and ESDs are generally connected to a medium voltage DC (MVDC) grid. The current level in the case of the MVDC grid is low compared to the medium voltage AC (MVAC) grid which ensures lower conduction losses [6], [7]. Moreover, The functionalities like voltage regulation, power flow control, current limitation, fault detection, and isolation are also added advantages of using an MVDC grid [8]. Thus, the MVDC grid is more suitable for integrating RES and ESD. However, for the integration of RES/ESD to the MVDC grid, a bi-directional DC-DC converter (BDC) plays an important role.

Throughout the years of investigation, several BDCs are proposed in the literature, which is broadly classified in two categories, namely, non-isolated [9]–[15] and isolated converters [16]–[20]. All of them have their benefits and applications, but among them, dual active bridge converters (DAB) has

drawn significant attention of the researchers due to (1) high-frequency galvanic isolation between the input to output port, (2) high voltage gain, (3) high power handling capability, (4) soft switching commutation, (5) compact size, and (6) high efficiency [18].

The conventional DAB converters use higher-rated MOSFET/IGBT switches for high-power applications. However, these switches experience significant voltage stress in the high voltage (HV) side of the high-frequency transformer (HFT) and increases the cost and size of the converter. The efficiency is also reduced due to huge conduction loss. A modified dual active bridge converter (m-DABC) with a neutral point clamp (NPC) structure on the HV side can be used to reduce this voltage stress, and to further increase the voltage gain, the NPC can be used as a voltage doubler circuit [21]–[23].

The converter performance also depends on the controller designed for its operation. The conventional proportional-integral (PI) control with feed-forward and proportional-integral-resonant (PIR) controller is widely used in the industry [24]–[26], but they fail to operate for a wide range of operations and under uncertain disturbances. A non-linear and sliding mode control (SMC) technique is proposed in [27], [28] which can address the disturbances caused by the input, output, or parameter variation. However, this requires detailed knowledge of all the state information of the system. In [29] a model-based phase-shift control (MPSC) strategy is implemented with feedback and loads current feed-forward regulators. The technique provides a fast dynamic response but still requires detailed knowledge of the system, and parameter sensitivity issues still persist. To make the system more robust with minimum information requirements, an adaptive control method can be applied. The most common adaptive control technique used in aerospace technology and other fields of control engineering is model reference adaptive control (MRAC) [30]–[33]. The advantage of this control method is that it can easily cancel the problems associated with parameter dependencies, operating point changes, and input variations without knowing the exact parameter details of the system. The controller adapts its feedback parameters online to control the plant output to match the reference. In this article, an MRAC based adaptive power management system (APMS) is presented for the m-DABC to integrate battery energy storage system (BESS) to the DC grid.

The rest of the article is organized as follows. In Section II, the circuit description, operation, modeling, and selection of the circuit parameters are discussed. The detailed design of the controller and its stability and convergence analysis are described in Section III. The simulation results and experimental findings are presented in Sections IV and V, respectively. Finally, in Section VI, a conclusion of the work has been drawn.

II. BIDIRECTIONAL MODIFIED DUAL ACTIVE BRIDGE CONVERTER

A. Circuit Description

The architecture of the modified dual active bridge converter has been shown in Fig. 1a. As can be seen in Fig. 1a, a

conventional H-bridge structure denoted as the base cell is connected to the low voltage (LV) side of the HFT, whereas the HV side is connected to an NPC structure which doubles the voltage at the output. The equivalent winding resistance and leakage inductance of the HFT referred to LV side are denoted by R_L and L_r , respectively. The combined voltage across the capacitors $C_{B1} = C$ and $C_{B2} = C$ together form the DC-link voltage v_{dc} . The LV side of the converter is connected to a battery energy storage v_{Batt} .

B. Circuit Operation

The converter is capable of delivering power in both directions. In this article, if power flows from battery storage to the grid, it is regarded as positive power flow, and if power flows from the grid to battery storage, it is regarded as negative power flow. The switches connected to the LV and HV winding of the HFT are operated by square pulse signals with a 50% duty cycle. These pulses are given in such a manner that they produce square wave voltages on the LV and HV sides of the HFT, which are phase shifted by an angle δ . This phase shift angle δ decides the magnitude and direction of the power flow (P) through the converter and is given in (1).

$$P = \frac{N_p}{N_s} \frac{V_{Batt} V_{dc} \delta (\pi - |\delta|)}{2\pi\omega L_r}. \quad (1)$$

where, $\frac{N_p}{N_s}$ is the turns ratio of the HFT and ω is the angular switching frequency of the converter. This method of operation is termed as single phase shift modulation technique, although other advanced modulation techniques are also easily applicable to the proposed m-DABC. The winding voltage waveform of the HFT and LV side current waveform for a positive power flow condition is showcased in Fig. 1b.

C. Reduced Order Harmonic Model of the m-DABC

A dynamic model based on harmonic analysis of the voltage waveform of the m-DABC is developed in [23]. In this modeling all the switches are assumed to be ideal. The DC-link voltage dynamics based on the Fourier series is derived as

$$\dot{v}_{dc} = f(v_{dc}) + b_p u. \quad (2)$$

where,

$$f(v_{dc}) = -\frac{2v_{dc}}{R_{load}C} = -a_p v_{dc} \quad (3)$$

$$b_p = \frac{16}{C\pi^2} \frac{N_p}{N_s} \sum_{m=0}^{\infty} \frac{1}{[2m+1]^2} \frac{v_{Batt}}{|Z[m]|} \quad (4)$$

$$|Z[m]| = \sqrt{R_L^2 + ([2m+1]\omega L_r)^2} \quad (5)$$

$$u = \sin[2m+1]\delta \quad (6)$$

and m is the harmonic order. R_{load} is the output resistance and is determined as $R_{load} = v_{dc}/i_{load}$, with i_{load} being the load current. Equation (2) indicates that the characterizing transfer function of the m-DABC is of the first order. So, the model required for the design of the MRAC controller in the next section can be designed to be a first order model to compare with.

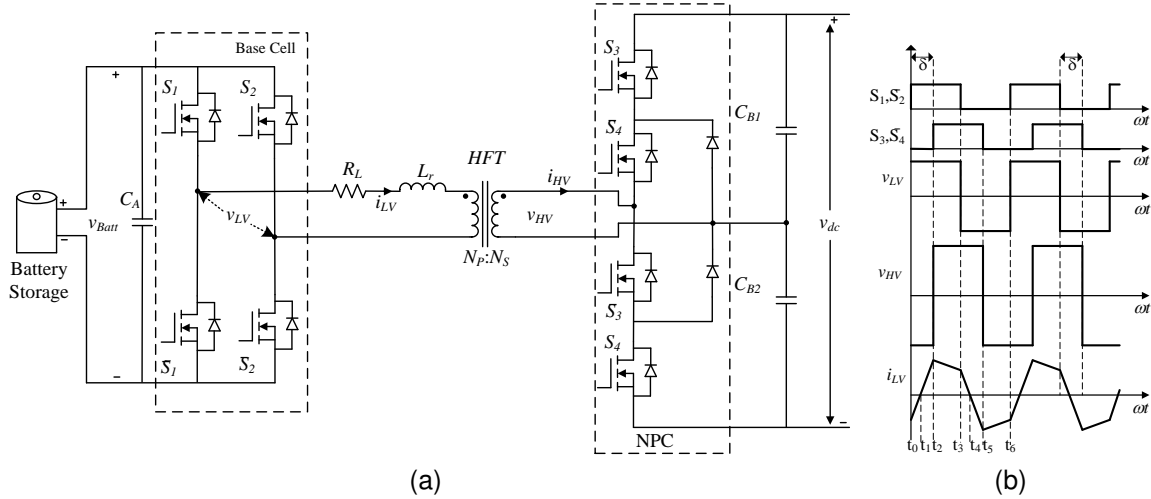


Fig. 1. (a) Architecture of m-DABC, (b) Waveforms of winding voltages and LV side current of HFT.

D. Choice of m-DABC parameters

The effectiveness of the m-DABC depends a lot on the choice of parameters. Depending on the leakage inductance L_r , the zero voltage switching (ZVS) operation of the switches of the converter is affected. For a perfect ZVS operation, two conditions must be satisfied, 1) the parasitic capacitor of the switch must be fully discharged to opposite polarity within available time by the energy stored in the leakage inductor L_r and 2) the dead time allocated for voltage transition must be four times the resonating time period [21]. From these two conditions, it can be formulated that,

$$T_d \geq \frac{\pi}{2} \sqrt{L_r C_z} \quad (7)$$

$$L_r I_{LV}^2 \geq C_z V_{Batt_{max}}^2 \quad (8)$$

where, T_d is the delay time required for the transition of voltage in the circuit and $C_z = 2C_s$, C_s being the output capacitance of the MOSFETs. From (8), L_r can be calculated.

III. ADAPTIVE POWER MANAGEMENT SYSTEM

The objective of the adaptive power management system (APMS) is to control the magnitude and direction of the power flow through the converter based on the requirement of the system. A droop control characteristic approach has been adopted to determine the reference signal of the controller. The detailed control scheme is presented in Fig. 2a. The APMS consists of a model reference adaptive voltage controller (MRAC) and a secondary droop voltage controller. The droop voltage controller takes power requirement information from the system and decides the allowable voltage deviation. This deviated voltage acts as the reference input to the MRAC voltage controller. The reference model response is compared with the plant output. The error and the reference input are fed to an adaptation law mechanism that estimates the control parameters for the control law at that operating condition. The output of the control law generates the desired phase shift angle δ to match the power requirement and maintain the DC link voltage. If the operating conditions change, even then, the controller imitates the reference model, and hence the system

performance remains almost unaltered. The detailed design of the control parts is described below.

A. Reference Model Design

The plant model is derived as a first order transfer function. So, the reference model whose behavior needs to be tracked is considered a first order system as given in (9).

$$\dot{v}_m = -a_m v_m + b_m v_r. \quad (9)$$

where, a_m and b_m are constant parameters that decide the system characteristics, v_m is the reference model output, and v_r is a bounded reference signal which is estimated based on the power flow command. The parameters a_m and b_m are strictly positive to make the system stable. The corresponding transfer function of the reference model is derived as a strictly positive real (SPR) function as given in (10).

$$W_m = \frac{V_m}{V_r} = \frac{b_m}{s + a_m}. \quad (10)$$

B. Voltage Controller Design

The voltage controller design is divided into two parts, i.e., formulating (1) a control law and (2) an adaptive law. The primary objective of the controller is to ensure that the error between the reference model output voltage and actual plant output voltage ($e = v_{dc} - v_m$) converges to zero asymptotically. It is achieved by considering the sign of b_m to be known. In the model of m-DABC it can be seen that for all real values of system parameters, b_p is strictly positive, and thus it can be assumed that b_m is also positive.

1) *Control Law Design*: In this work, the control law is chosen such that it allows a perfect convergence, and it is formulated as

$$u = \tilde{a}_r v_r + \tilde{a}_y v_{dc}. \quad (11)$$

where, \tilde{a}_r and \tilde{a}_y are feedback gains of the system. The closed loop system dynamics with this control law is derived as

$$\dot{v}_{dc} = -(a_p - \tilde{a}_y b_p) v_{dc} + \tilde{a}_r b_p v_r. \quad (12)$$

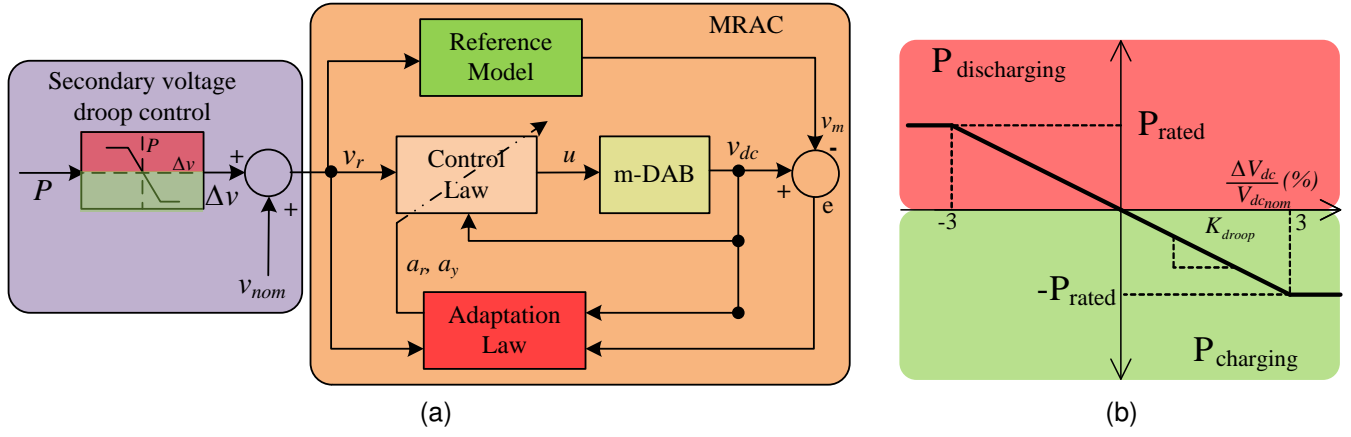


Fig. 2. (a) Architecture of the APMS, (b) Droop characteristic of the system.

For perfect tracking, i.e., $e = v_{dc} - v_m = 0$, and from (9) and (12), the estimated control parameters can be found to be

$$a_r^* = \frac{b_m}{b_p}, \quad a_y^* = \frac{a_p - a_m}{b_p}. \quad (13)$$

In (11), the first term provides the ideal DC gain, and the second term replaces the pole $-a_p v_{dc}$ with $-a_m v_{dc}$.

In this work, a_p and b_p are assumed to be unknown, and depending on the operating point; the control parameters are varied in an adaptive fashion according to the adaptation law. Based on the tracking error, the adaptation law estimates the suitable gain so as to converge the system.

2) *Adaptation Law Design*: The control parameters \tilde{a}_r and \tilde{a}_y are estimated online based on the operating condition of the system to track the reference model output. The tracking error of the system is chosen as $e = v_{dc} - v_m$. For a non-zero tracking error, the control parameter error is then given as,

$$\hat{a} = \begin{bmatrix} \hat{a}_r \\ \hat{a}_y \end{bmatrix} = \begin{bmatrix} \tilde{a}_r - a_r^* \\ \tilde{a}_y - a_y^* \end{bmatrix}. \quad (14)$$

The dynamics of the tracking error is found from (9) and (12) as

$$\begin{aligned} \dot{e} &= -a_m(v_{dc} - v_m) \\ &\quad + (a_m - a_p + b_p \tilde{a}_y)v_{dc} + (b_p \tilde{a}_r - b_m)v_r \\ &= -a_m e + b_p(\hat{a}_r v_r + \hat{a}_y v_{dc}). \end{aligned} \quad (15)$$

Applying Laplace Transform on (15), the tracking error can be represented as

$$E = \frac{b_p(\hat{a}_r V_r + \hat{a}_y V_{dc})}{s + a_m} = \frac{W_m(\hat{a}_r V_r + \hat{a}_y V_{dc})}{a_r^*}. \quad (16)$$

The objective of the adaptation law is to change the control parameters in the direction of the negative gradient of a Lyapunov candidate function $J(e, \hat{a})$ which is chosen as

$$J(e, \hat{a}) = 0.5[e^2 + \frac{|b_p|}{\gamma}(\hat{a}_r^2 + \hat{a}_y^2)] \quad (17)$$

Based on (16) and (17), the adaptation law can be deduced as follows.

$$\begin{aligned} \dot{\hat{a}}_r &= -\text{sgn}(b_p)\gamma v_r e \\ \dot{\hat{a}}_y &= -\text{sgn}(b_p)\gamma v_{dc} e \end{aligned} \quad (18)$$

where, γ is a positive constant known as adaptive gain, and $\text{sgn}(b_p)$ determines the direction of search for accurate control parameters for perfect tracking.

Alternately, some other modern control techniques like sliding mode control (SMC), model predictive control (MPC), or LQR control with integral action can also imitate similar performance. However, they require either initial state information or extensive computation. Moreover, their accuracy depends on the parameter adaptation algorithm, which still does not guarantee the same dynamic behavior at all operating points.

C. Secondary Voltage Droop Control

A secondary droop control is also designed to improve the dynamic behavior of the system response. The droop controller shifts the reference voltage V_r of the MRAC in accordance with the power flow. The relation between power and droop voltage is expressed in Fig. 2b. For a forward power flow from ESD to the DC bus, the voltage deviation is negative whereas, for reverse power flow, it is positive. This implies that when the DC bus voltage falls/rises up to 3% of the nominal value, the power will be delivered from/to the ESD, and the APMS will maintain the DC link voltage at the modified reference voltage.

D. Stability and Tracking Convergence Analysis

The stability and convergence characteristic of the system is analyzed based on the Lyapunov stability theory and Barbalat's lemma, which states that for a positive definite function $f(x, t)$ with a finite limit as $t \rightarrow \infty$, if $\dot{f}(x, t)$ is negative semi-definite and uniformly continuous for all $t \in [0, \infty)$, then $f(x, t) \rightarrow 0$ as $t \rightarrow \infty$.

The derivative of the Lyapunov function (17) is derived as

$$\begin{aligned} \dot{J}(e, \hat{a}) &= e\dot{e} + \frac{|b_p|\tilde{a}_r\dot{\tilde{a}}_r}{\gamma} + \frac{|b_p|\tilde{a}_y\dot{\tilde{a}}_y}{\gamma} = -a_m e^2 \\ &\quad + \hat{a}_r(|b_p|\frac{\dot{\tilde{a}}_r}{\gamma} + b_p v_r e) + \hat{a}_y(|b_p|\frac{\dot{\tilde{a}}_y}{\gamma} + b_p v_{dc} e) \end{aligned} \quad (19)$$

Since, $b_p = |b_p| \text{sgn}(b_p)$, then (19) can be further simplified to

$$\begin{aligned} \dot{J}(e, \hat{a}) = & -a_m e^2 + |b_p| \hat{a}_r \left(\frac{\dot{\hat{a}}_r}{\gamma} + \text{sgn}(b_p) v_r e \right) \\ & + |b_p| \hat{a}_y \left(\frac{\dot{\hat{a}}_y}{\gamma} + \text{sgn}(b_p) v_{dc} e \right) \end{aligned} \quad (20)$$

As a_r^* and a_y^* are constant control parameters for a particular operating point, from (14), it can be shown that $\dot{\hat{a}}_r = \dot{a}_r$ and $\dot{\hat{a}}_y = \dot{a}_y$. Thus, with the chosen adaptation law in (18) and from (20), it can be shown that $\dot{J}(e, \hat{a}) = -a_m e^2 \leq 0$. Hence, the adaptive control system is proved to be globally stable as e , \hat{a}_r , and \hat{a}_y are bounded. Moreover, the boundedness of e , \hat{a}_r , and \hat{a}_y indicates the boundedness of \dot{e} (as per (15)) and uniform continuity of $\dot{J}(e, \hat{a})$, which in turn ensures the global asymptotic convergence of the tracking error e according to Barbalat's lemma.

IV. SIMULATION RESULTS

The m-DABC, along with the MRAC controller, has been simulated in MATLAB/SIMULINK environment to verify its effectiveness. The parameters used in the simulation are given in Table I. In the presented work, the reference model is designed for a time constant of $1.72ms$, a settling time of $6.9ms$, and a rise time of $3.8ms$. The performance of the system with conventional PI control, single integral sliding mode control (SMC), and APMS have been investigated in the simulation. The effect of different power flow conditions, source voltage, and parametric variation are compared below for all three controllers.

TABLE I
SYSTEM PARAMETERS

| Symbol | System Parameter | Value |
|--------------|---------------------------|---------|
| P_{nom} | Nominal power rating | 500W |
| V_{Batt} | Battery voltage | 48V |
| $V_{dc,nom}$ | Nominal DC link Voltage | 249.6V |
| L_r | Inductor | 1.54μH |
| C | Output capacitor | 500μF |
| $N_p : N_s$ | Turns ratio of HFT | 1 : 2.5 |
| f_s | Switching frequency | 50kHz |
| γ | Adaptation gain | 1 |
| a_m, b_m | Reference model parameter | 580 |
| K_{droop} | Voltage droop constant | 166.6 |

A. Source Voltage Disturbance Rejection

The converter and controller are simulated for variable input DC voltage with the conventional PI controller, SMC, and APMS. The corresponding results are shown in Fig. 3. The power flow from ESD to the DC bus has been kept constant at 320W during the changes in source voltage. The initial input voltage is kept at 48V, and from $t = 0.025s$, it is gradually decreased to 42V. Again, from $t = 0.1s$, the voltage is gradually increased to 48V. The gradual change in the source voltage has been considered instead of a step change

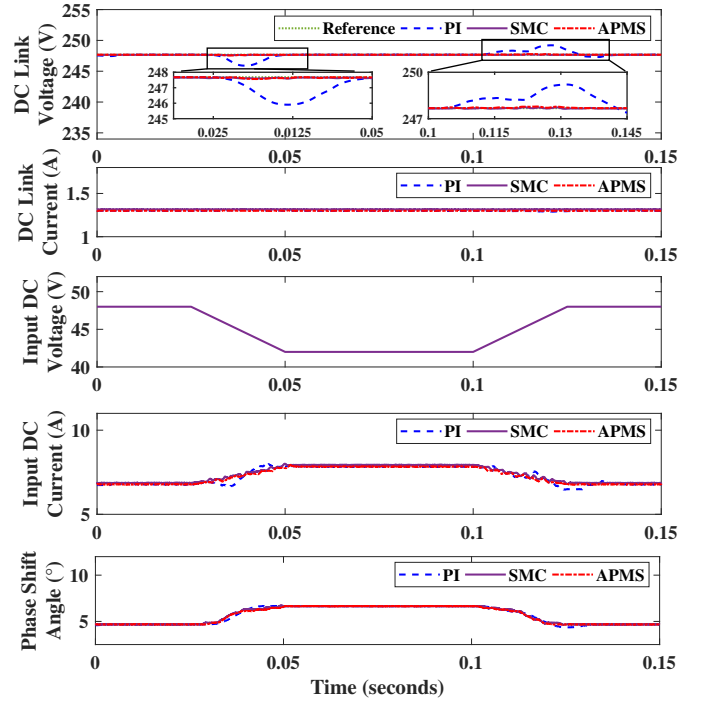


Fig. 3. Effect of source voltage variation.

to imitate the effect of the charging/discharging process of a battery. It can be seen from Fig. 3 that, during the changes in source voltage, the DC link voltage and current remain almost unaltered for SMC and APMS. The corresponding input current and phase shift angle of the converter is also shown in the figure. However, for the PI controller, the DC link voltage varies slightly during the changing period of the source voltage. Hence, the input DC current also changes accordingly to maintain the output power demand.

B. Load Disturbance Rejection

The effect of change in power flow conditions with conventional PI control technique, SMC, and APMS is investigated in simulation environment. The corresponding results are shown in Fig. 4. The source voltage during these conditions is kept unaltered at 48V. Initially, 100W power is being delivered to the DC bus, and at $t = 0.05s$, a step change in load has been made from 100W to 200W and back to 100W at $t = 0.1s$. Again, at $t = 0.15s$, the power flow is changed from $P = 100W$ to $P = 300W$ and back to 100W at $t = 0.2s$. It can be seen from the figure that during the step change in the load, the reference voltage of the DC bus is changed in accordance to the droop characteristic of the system and the voltage deviation is well within 3% of the nominal voltage. The output voltage of the converter also tracks the modified reference voltage efficiently. However, the steady state is reached within 25ms for a transition of power from 100W to 200W with the PI controller. The voltage overshoot for this case is observed to be 1.8V (0.72%). On the other hand, the settling time has been observed to be 10ms with a voltage overshoot of 0.5V (0.2%) and 0.3V (0.12%) for SMC and

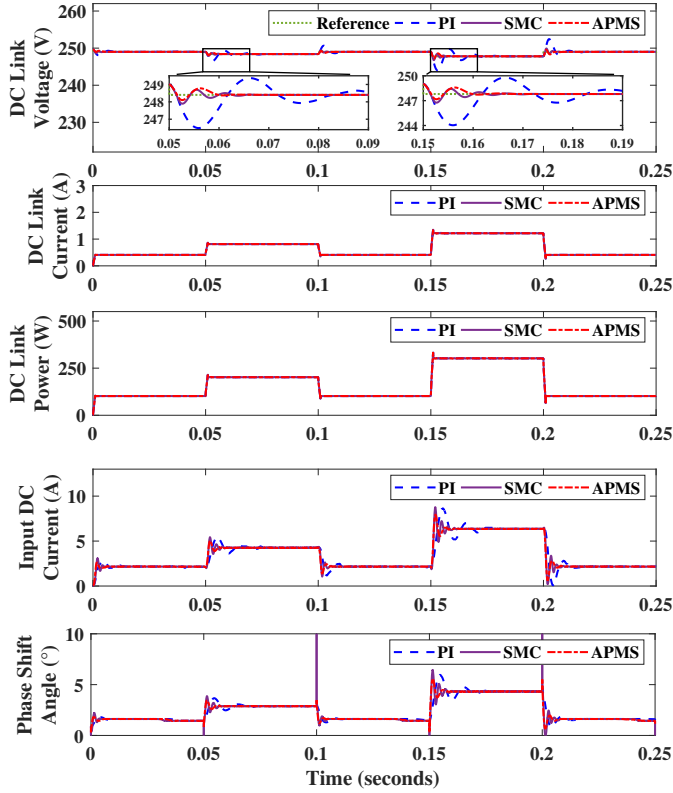


Fig. 4. Effect of load variation.

APMS, respectively. Moreover, for a step change in the power from 100W to 300W, the percentage overshoot is only 1V (0.4%) and 0.6V (0.24%) for SMC and APMS, respectively. The same disturbance caused an overshoot of 3.8V (1.5%) in the case of the PI controller. The corresponding DC link current and phase shift angle of the converter are also shown in the figure for all the controllers. It is also observed that the phase shift angle has a considerable overshoot for higher power flow in the case of the PI controller and SMC, which eventually produces disturbances in the system. However, the APMS produces a smoother phase shift angle throughout the simulation. Hence, it can be inferred from the results that the APMS showcases better performance than the conventional PI controller and SMC.

The voltage and current waveform at the LV side and voltage at the HV side of the HFT for APMS controller is shown in Fig. 5. The variation of the adaptive parameters a_r and a_y are also shown in Fig. 5, which show how the system adapts itself in the presence of the load disturbances.

C. Simultaneous Parameter and Load Disturbance Rejection

The effect of load variation under parameter mismatch conditions with the conventional PI controller, SMC, and APMS is also investigated in this work. An additional inductance of $1.54\mu H$ is inserted in series with the HFT winding for this purpose, and the power is varied from 100W to 300W and back to 100W. The effect of the inductance mismatch on the DC link voltage is shown in Fig. 6. It is observed

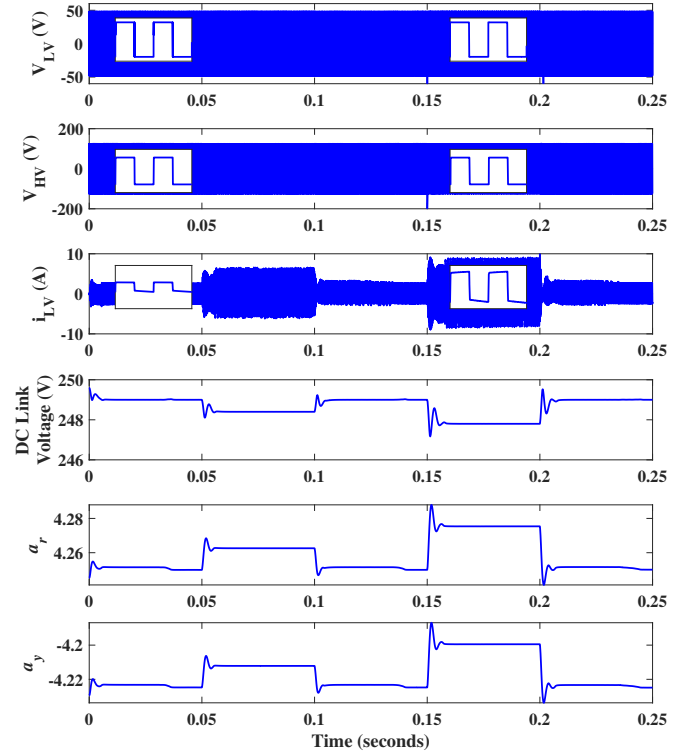


Fig. 5. Voltage and current waveform in the winding of HFT for different power with APMS.

that the settling time and overshoot for the DC link voltage with the PI controller change by $2.5ms$ and $1V$, respectively, for the same tuning parameters. Similarly, for the SMC, the settling time and voltage overshoot increased by $3ms$ and $0.5V$, respectively. However, they are not affected in the case of APMS, even without further tuning. The APMS rejects the effect of parameter mismatch as the adaptation parameters are changed automatically to follow the provided reference model.

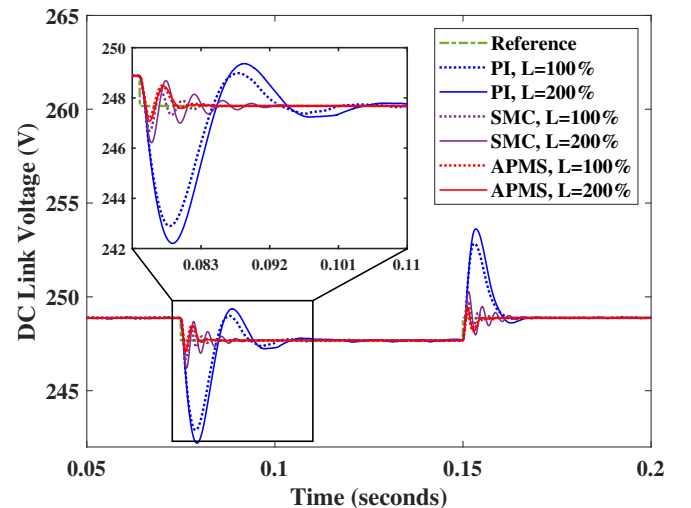


Fig. 6. Effect of load variation under parameter mismatch.

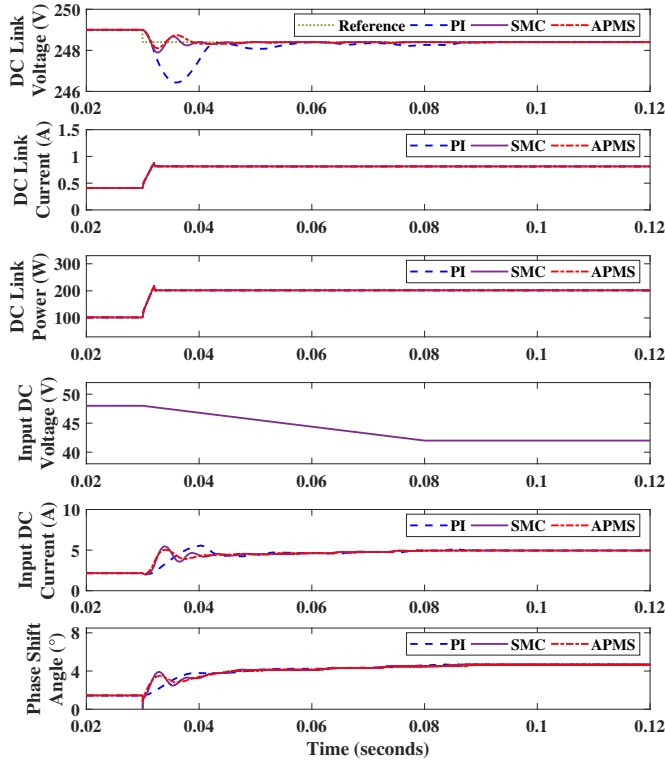


Fig. 7. Effect of simultaneous source and load disturbance.

D. Simultaneous Source and Load Disturbance Rejection

The effect of simultaneous source and load disturbance with the conventional PI controller, SMC, and APMS is shown in Fig. 7. The power flow requirement is increased from 100W to 200W at $t = 0.03s$. At the same time, input DC voltage is also reduced from 48V to 42V. It is observed that DC link voltage overshoot remains the same at 1.8V for PI controller, 0.5V for SMC, and 0.3V for APMS. However, the settling time increases slightly to 30ms for the PI controller and 12ms for SMC and APMS. The corresponding DC link current, input DC current, and phase shift angle are also shown in Fig. 7.

The simulation results prove that even under multiple disturbances, the system works efficiently with the proposed APMS technique.

V. EXPERIMENTAL RESULTS

TABLE II
COMPONENT LIST

| Component | Description |
|--------------------------|-----------------|
| LV side switching device | TK56A12N1 |
| HV side switching device | IXFP38N30X3M |
| Capacitor bank | MKP C4AQ |
| NPC clamping diodes | MUR460 |
| HF transformer winding | SWG40 Litz wire |
| Onboard voltage sensor | AMC1311DWVR |

The proposed system has also been verified on a 500 W laboratory prototype. The experimental circuit schematic along with its control methodology, is shown in Fig 8a. On the

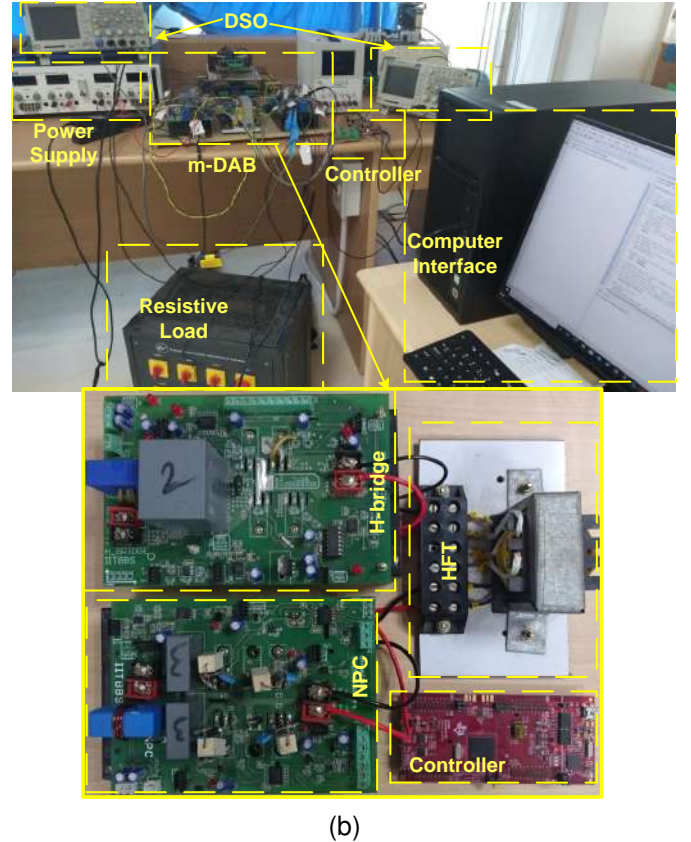
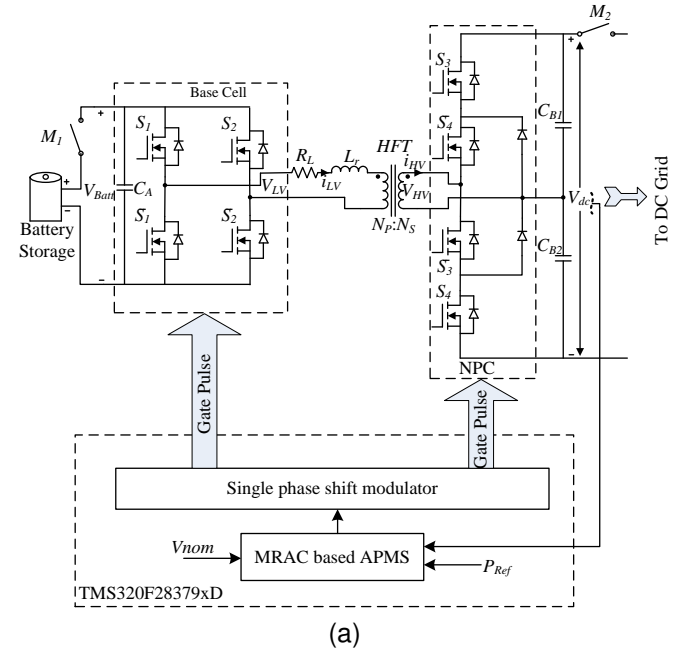


Fig. 8. (a) Complete system layout, (b) Experimental setup.

LV side of the converter, a programmable power supply has been used as a input DC power supply. The HV side of the converter is connected to the DC bus and a variable resistive load box is connected to it for changing load demands. When the miniature circuit breaker (MCB) M_1 is ON, the power supply is connected to the m-DABC LV side. Similarly, when MCB M_2 is ON, the DC bus is connected to the HV side.

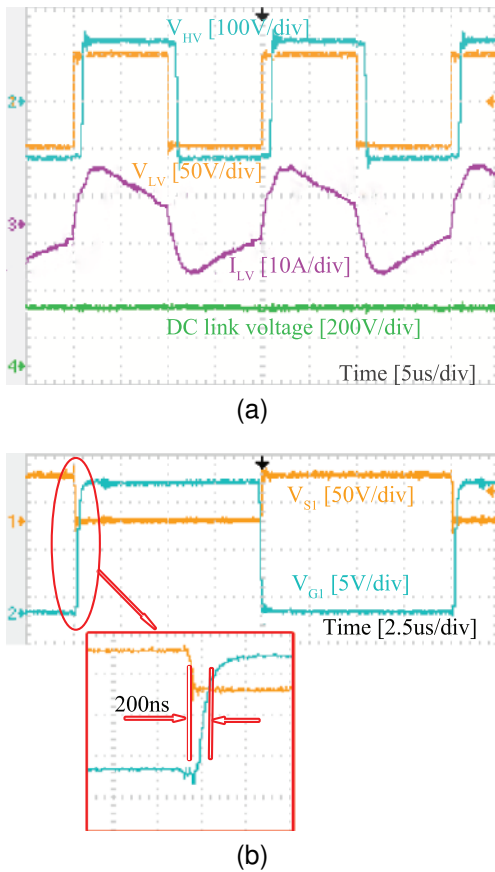


Fig. 9. (a) High frequency transformer voltage current and DC link voltage, (b) Zero voltage switching of S_1 .

The manual switches in the resistive load box provides stiff load change to the system.

The experimental prototype of the converter is shown in Fig. 8b. A TMS320F2837xD evaluation board from Texas Instruments has been utilized for designing the PI controller, SMC, and APMS that communicates to the host computer through the code composer studio compiler. The ePWM modules of TMS320F2837xD provide the gate pulses to the eight switches of the converter via isolated gate drivers ISO5452DW and IR2100. The remaining major components used in the setup are given in Table II. The overall system has been tested with the same circuit parameters as provided in Table I.

The experimental setup has been tested for different operating conditions to prove the effectiveness of the proposed APMS over conventional PI controller and SMC. The transformer LV side voltage, HV side voltage, LV side current, and DC link voltage are shown in Fig. 9a for the 347W power flow condition. The S_1 gate pulse and the voltage across the switch for the same power flow are shown in Fig. 9b, which confirms the zero voltage switching (ZVS) of the semiconductor device S_1 . The same phenomenon was observed for the remaining switches also.

The effect of input voltage variation has been shown in Fig. 10 for a constant power flow of 320W. It can be seen from the figures that, for a fall and rise in the source voltage from 48V to 42V and vice versa, the DC link voltage variation is negligible, and as a result, the current and power delivered

to the DC bus remains unaltered at 320W. However, it is also observed that for a higher range of input voltage variation, the conventional PI controller response is quite unsatisfactory compared to SMC and APMS. But, as this work focuses on the integration of a Li-ion battery into the system, it is evident that the battery management system (BMS) of the cell pack will disconnect the battery for a voltage lower than 42V. Hence, it can be inferred that within this range of source voltage variation, all the controller produces similar behavior.

Figure 11 indicates the effect of variation in the load at the DC bus voltage with PI controller, SMC, and APMS. The DC bus voltage corresponding to a positive power flow of 100W is 249V. The load change has been performed for 100W \rightarrow 200W \rightarrow 100W \rightarrow 300W \rightarrow 100W. As per the droop characteristic, the steady state value of the DC bus voltage changes as 249V \rightarrow 248.6V \rightarrow 249V \rightarrow 247.2V \rightarrow 249V. This voltage deviation is well within the 3% of the nominal value of the DC bus voltage as per the droop characteristic of the system. The settling time for the voltage signal was measured to be 20ms with an overshoot of 30V during the transition from 100W to 200W for the PI controller, as indicated in Fig. 11a. For a higher power rise from 100W to 300W, the settling time and overshoot increased to 60ms and (40–50V) as shown in Fig. 11d. The SMC improves the settling time to 10ms and 15ms with overshoot of 20V and 40V as shown in Fig. 11b and 11e respectively. However, the steady state is reached within 5ms and 10ms with an overshoot of 20V and 30V, respectively for APMS as can be seen in Fig. 11c and 11f. The experimental results prove a good dynamic behavior of the system with the proposed controller.

The effect of the parameter variation with PI controller, SMC, and APMS is also investigated and shown in Fig. 12. The leakage inductance of the HFT is increased to double by introducing an additional inductor in series with the transformer winding. The effect of load variation from 100W to 300W with this parameter mismatch condition is then investigated. It is observed that for the conventional PI controller, the DC link voltage overshoot becomes 72V with a settling time of 25ms, as seen in Fig. 12a. However, the SMC and APMS maintain almost the same settling time of 15ms and 10ms with a slight increase in DC link voltage overshoot to 50V and 40V as shown in Fig. 12b and 12c respectively.

A comparison of the three control method for a simultaneous variation of source DC voltage and load is also investigated, and the corresponding results are shown in Fig. 13. The source DC voltage is varied gradually from 48V to 42V, and at the same time, the load power demand was changed from 100W to 200W. It is observed that the DC link voltage overshoot remains almost unaltered, whereas the settling time changes slightly to 25ms for the PI controller and 15ms for SMC. However, it remains the same at 5ms with APMS.

The experimental findings show the effectiveness of the proposed converter and the APMS for different operating conditions with the adaptive feature for better performance.

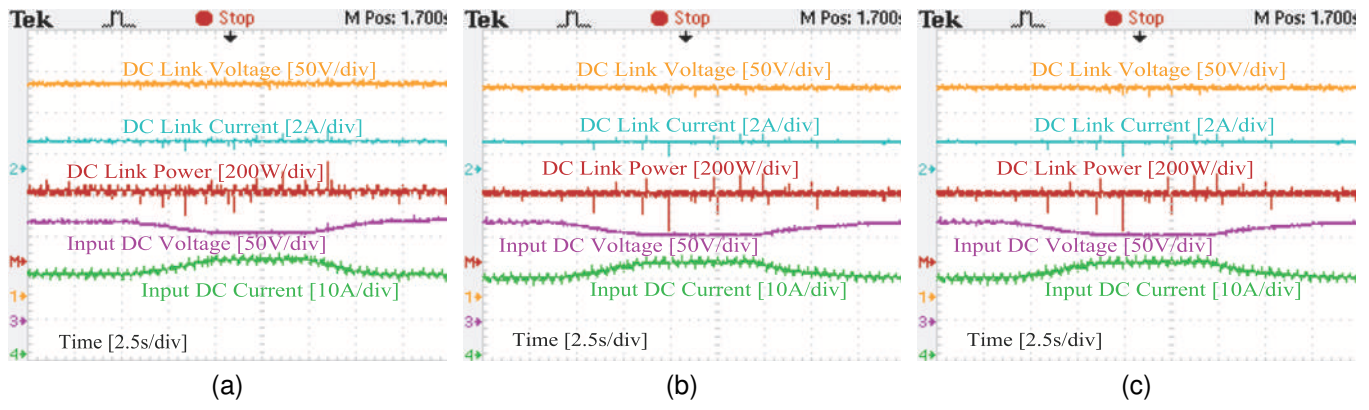


Fig. 10. Effect of variation in input voltage with (a) PI controller, (b) SMC, (c) APMS.

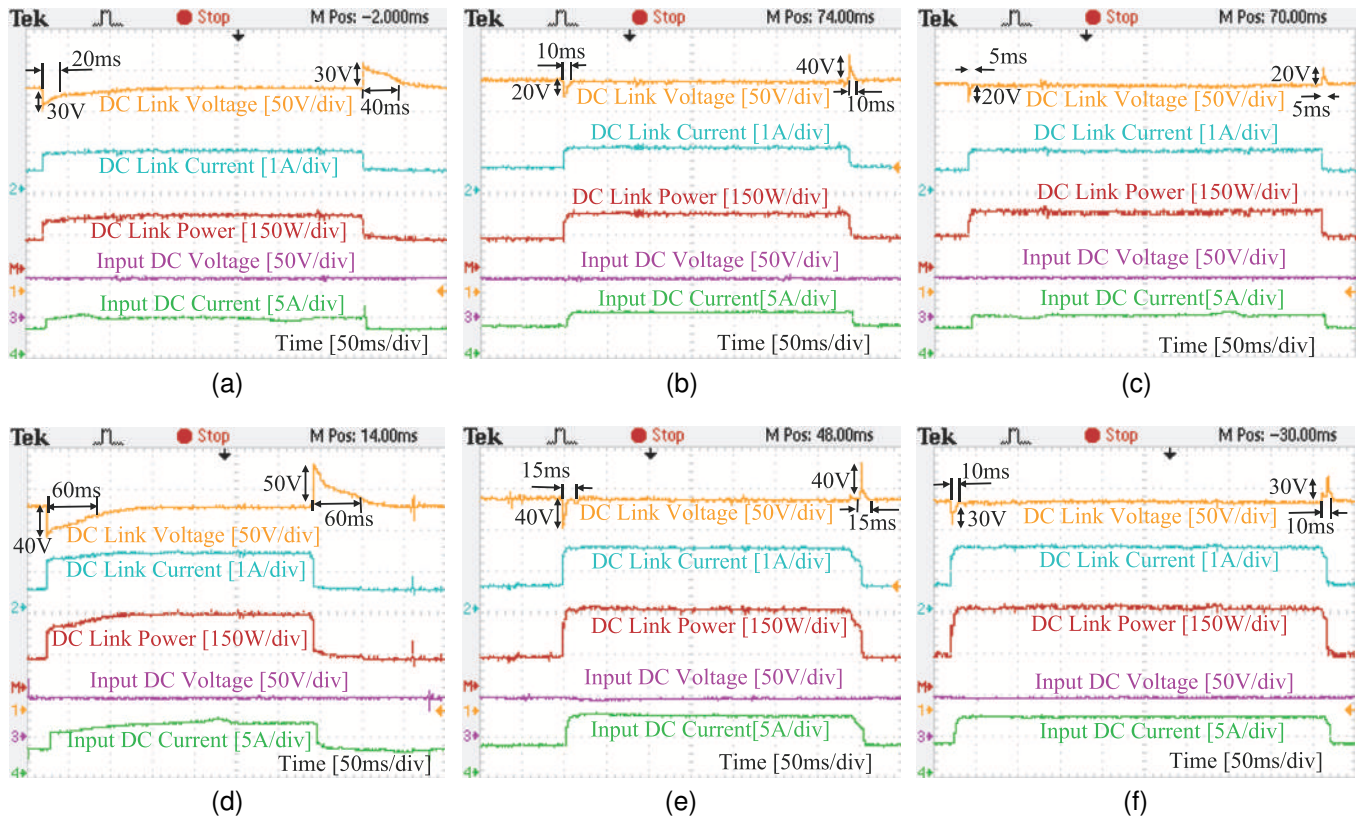


Fig. 11. Effect of load change for $P = 100W \leftrightarrow 200W$ with (a) PI controller, (b) SMC, (c) APMS, and for $P = 100W \leftrightarrow 300W$ with (d) PI controller, (e) SMC, (f) APMS.

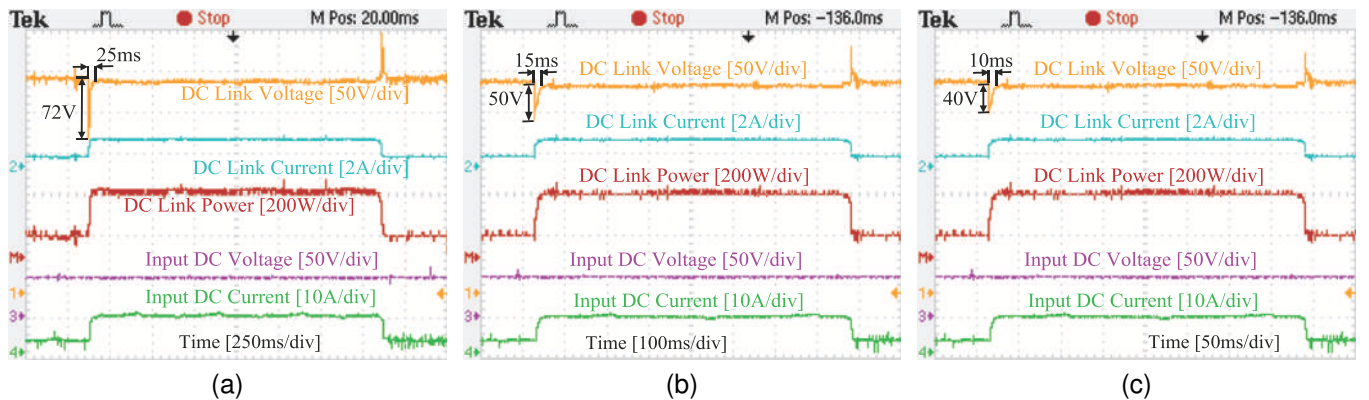


Fig. 12. Effect of simultaneous variation in inductance and load with (a) PI controller, (b) SMC, (c) APMS.

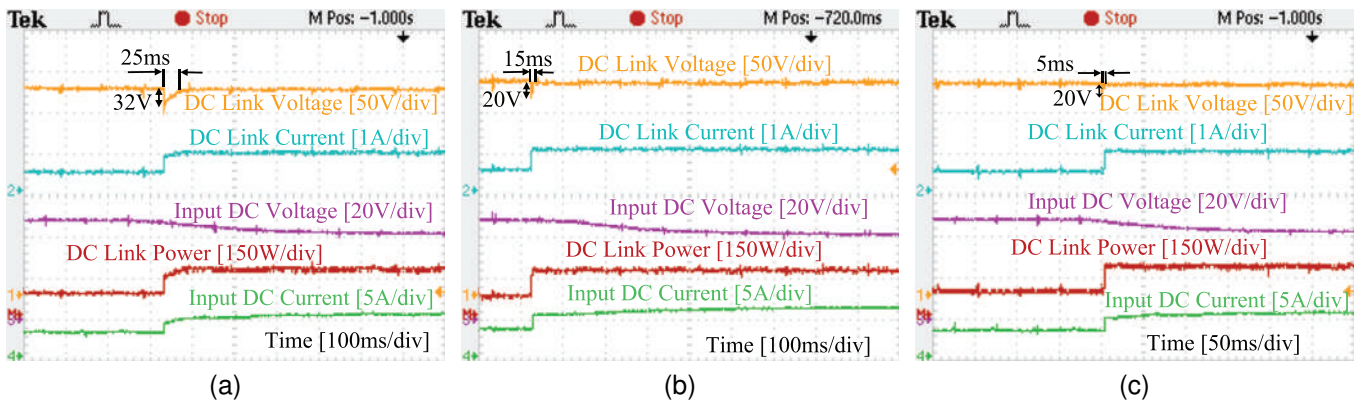


Fig. 13. Effect of simultaneous source and load variation with (a) PI controller, (b) SMC, (c) APMS.

VI. CONCLUSION

In this article, an APMS is presented for an m-DAB converter operating under a single phase shift mode. The APMS is designed based on droop control and model reference adaptive control. The adaptive feature of the APMS eliminates the requirement of detailed knowledge of the converter and maintains a superior dynamic performance. The APMS estimates the control parameters online for different operating conditions and under disturbances which proves the robustness of the controller. Stability analysis of the implemented controller is also carried out based on Lyapunov stability theory. Finally, the system is tested in simulation and the real-time environment with a conventional PI controller, sliding mode controller, and proposed APMS for different operating conditions and under multiple disturbances. The results are presented to showcase the advantage of the proposed APMS over the conventional PI controller and SMC.

In future work, the proposed adaptive power management system could be further improved to suppress the effect of sensor noise. The proposed APMS might be incorporated with a controller bandwidth parameter that can filter out the noise present in the feedback signal. The associated stability analysis need also be investigated for the modification. Moreover, a seamless transition mechanism from single phase shift to dual phase shift mode and vice-versa could be investigated for different voltage gains of the converter.

REFERENCES

- [1] K. Hansen, C. Breyer, and H. Lund, "Status and perspectives on 100% renewable energy systems," *Energy*, vol. 175, pp. 471–480, 2019.
- [2] M. Bazilian, T. Mai, S. Baldwin, D. Arent, M. Miller, and J. Logan, "Decision-making for high renewable electricity futures in the united states," *Energy Strategy Reviews*, vol. 2, no. 3-4, pp. 326–328, 2014.
- [3] P. D. Lund, J. Lindgren, J. Mikkola, and J. Salpakari, "Review of energy system flexibility measures to enable high levels of variable renewable electricity," *Renewable and sustainable energy reviews*, vol. 45, pp. 785–807, 2015.
- [4] A. S. Brouwer, M. Van Den Broek, A. Seebregts, and A. Faaij, "Impacts of large-scale intermittent renewable energy sources on electricity systems, and how these can be modeled," *Renewable and Sustainable Energy Reviews*, vol. 33, pp. 443–466, 2014.
- [5] J. Hu, R. Harmsen, W. Crijns-Graus, E. Worrell, and M. van den Broek, "Identifying barriers to large-scale integration of variable renewable electricity into the electricity market: A literature review of market design," *Renewable and Sustainable Energy Reviews*, vol. 81, pp. 2181–2195, 2018.
- [6] M. Stieneker and R. W. De Doncker, "Medium-voltage dc distribution grids in urban areas," in *2016 IEEE 7th international symposium on power electronics for distributed generation systems (PEDG)*. IEEE, 2016, pp. 1–7.
- [7] M. Abbasi and J. Lam, "A step-up transformerless, zv-zcs high-gain dc/dc converter with output voltage regulation using modular step-up resonant cells for dc grid in wind systems," *IEEE Journal of Emerging and Selected Topics in Power Electronics*, vol. 5, no. 3, pp. 1102–1121, 2017.
- [8] M. S. Agamy, D. Dong, L. J. Garcés, Y. Zhang, M. E. Dame, X. Wu, and Y. Pan, "A high power medium voltage resonant dual active bridge for mvdc ship power networks," *IEEE Journal of Emerging and Selected Topics in Power Electronics*, vol. 5, no. 1, pp. 88–99, 2016.
- [9] H. Matsuo and F. Kurokawa, "New solar cell power supply system using a boost type bidirectional dc-dc converter," *IEEE transactions on Industrial Electronics*, no. 1, pp. 51–55, 1984.
- [10] F. Caricchi, F. Crescimbeni, F. G. Capponi, and L. Solero, "Study of bi-directional buck-boost converter topologies for application in electrical vehicle motor drives," in *APEC'98 Thirteenth Annual Applied Power Electronics Conference and Exposition*, vol. 1. IEEE, 1998, pp. 287–293.
- [11] J. Majo, L. Martinez, A. Poveda, L. G. de Vicuna, F. Guinjoan, A. F. Sanchez, M. Valentin, and J. C. Marpinard, "Large-signal feedback control of a bidirectional coupled-inductor cuk converter," *IEEE Transactions on Industrial Electronics*, vol. 39, no. 5, pp. 429–436, 1992.
- [12] M.-S. Song, Y.-D. Son, and K.-H. Lee, "Non-isolated bidirectional soft-switching sepic/zeta converter with reduced ripple currents," *Journal of Power Electronics*, vol. 14, no. 4, pp. 649–660, 2014.
- [13] H.-S. Lee and J.-J. Yun, "High-efficiency bidirectional buck-boost converter for photovoltaic and energy storage systems in a smart grid," *IEEE Transactions on Power Electronics*, vol. 34, no. 5, pp. 4316–4328, 2018.
- [14] A. Kushnerov and S. Ben-Yaakov, "Algebraic synthesis of fibonacci switched capacitor converters," in *2011 IEEE International Conference on Microwaves, Communications, Antennas and Electronic Systems (COMCAS 2011)*. IEEE, 2011, pp. 1–4.
- [15] F. Z. Peng, F. Zhang, and Z. Qian, "A magnetic-less dc-dc converter for dual-voltage automotive systems," *IEEE Transactions on Industry Applications*, vol. 39, no. 2, pp. 511–518, 2003.
- [16] F. Zhang, L. Xiao, and Y. Yan, "Bi-directional forward-flyback dc-dc converter," in *2004 IEEE 35th Annual Power Electronics Specialists Conference (IEEE Cat. No. 04CH37551)*, vol. 5. IEEE, 2004, pp. 4058–4061.
- [17] M. Cacciato, F. Caricchi, F. Giuhlii, and E. Santini, "A critical evaluation and design of bi-directional dc/dc converters for super-capacitors interfacing in fuel cell applications," in *Conference Record of the 2004 IEEE Industry Applications Conference, 2004. 39th IAS Annual Meeting*, vol. 2. IEEE, 2004, pp. 1127–1133.
- [18] F. Krismer and J. W. Kolar, "Efficiency-optimized high-current dual active bridge converter for automotive applications," *IEEE Transactions on Industrial Electronics*, vol. 59, no. 7, pp. 2745–2760, 2011.
- [19] P. He and A. Khaligh, "Comprehensive analyses and comparison of 1 kw isolated dc-dc converters for bidirectional ev charging systems," *IEEE Transactions on Transportation Electrification*, vol. 3, no. 1, pp. 147–156, 2016.

- [20] M. Moonem, C. Pechacek, R. Hernandez, and H. Krishnaswami, "Analysis of a multilevel dual active bridge (ml-dab) dc-dc converter using symmetric modulation," *Electronics*, vol. 4, no. 2, pp. 239–260, 2015.
- [21] S. B. Karanki and D. Xu, "Voltage droop control of dual active bridge for integrating battery energy storage to utility grid," in *2014 IEEE Energy Conversion Congress and Exposition (ECCE)*. IEEE, 2014, pp. 2227–2232.
- [22] G. Ortiz, M. G. Leibl, J. E. Huber, and J. W. Kolar, "Design and experimental testing of a resonant dc-dc converter for solid-state transformers," *IEEE Transactions on Power Electronics*, vol. 32, no. 10, pp. 7534–7542, 2016.
- [23] S. K. Mitra and S. B. Karanki, "A grid integrated bi-directional dual active bridge converter with model reference adaptive control based power flow controller," in *2019 National Power Electronics Conference (NPEC)*. IEEE, 2019, pp. 1–5.
- [24] H. Qin and J. W. Kimball, "Closed-loop control of dc-dc dual-active-bridge converters driving single-phase inverters," *IEEE transactions on power electronics*, vol. 29, no. 2, pp. 1006–1017, 2013.
- [25] Z. Shan, J. Jatskevich, H. H.-C. Iu, and T. Fernando, "Simplified load-feedforward control design for dual-active-bridge converters with current-mode modulation," *IEEE Journal of Emerging and Selected Topics in Power Electronics*, vol. 6, no. 4, pp. 2073–2085, 2018.
- [26] D. Das, S. Mishra, and B. Singh, "Design architecture for continuous-time control of dual active bridge converter," *IEEE Journal of Emerging and Selected Topics in Power Electronics*, vol. 9, no. 3, pp. 3287–3295, 2020.
- [27] D. D. M. Cardozo, J. C. Balda, D. Trowler, and H. A. Mantooth, "Novel nonlinear control of dual active bridge using simplified converter model," in *2010 Twenty-Fifth Annual IEEE Applied Power Electronics Conference and Exposition (APEC)*. IEEE, 2010, pp. 321–327.
- [28] Y.-C. Jeung and D.-C. Lee, "Voltage and current regulations of bidirectional isolated dual-active-bridge dc-dc converters based on a double-integral sliding mode control," *IEEE Transactions on Power Electronics*, vol. 34, no. 7, pp. 6937–6946, 2018.
- [29] W. Zhao, X. Zhang, S. Gao, and M. Ma, "Improved model-based phase-shift control for fast dynamic response of dual-active-bridge dc/dc converters," *IEEE Journal of Emerging and Selected Topics in Power Electronics*, vol. 9, no. 1, pp. 223–231, 2021.
- [30] L. Sun, "Helicopter hovering control design based on model reference adaptive method," in *2019 IEEE 3rd Information Technology, Networking, Electronic and Automation Control Conference (ITNEC)*. IEEE, 2019, pp. 1621–1624.
- [31] J. Chen, J. Wang, and W. Wang, "Model reference adaptive control for a class of aircraft with actuator saturation," in *2018 37th Chinese Control Conference (CCC)*. IEEE, 2018, pp. 2705–2710.
- [32] C. Ma, J. Lam, and F. L. Lewis, "Trajectory regulating model reference adaptive controller for robotic systems," *IEEE Transactions on Control Systems Technology*, vol. 27, no. 6, pp. 2749–2756, 2018.
- [33] X. Huang, C. Wu, and Y. Liu, "Finite-time h_∞ model reference control of slpv systems and its application to aero-engines," *IEEE Access*, vol. 7, pp. 43 525–43 533, 2019.